

Impact Study of Numerical Discretization Accuracy on Parameter Reconstructions and Model Parameter Distributions

Matthias Plock^a, Martin Hammerschmidt^{a,b}, Sven Burger^{a,b,†}, Philipp-Immanuel Schneider^{a,b},
and Christof Schütte^a

^a*Zuse Institute Berlin, Takustraße 7, 14195 Berlin, Germany*

^b*JCMwave GmbH, Bolivarallee 22, 14050 Berlin, Germany*

[†]*Corresponding author: burger@zib.de*

March 31, 2023

Abstract

Numerical models are used widely for parameter reconstructions in the field of optical nano metrology. To obtain geometrical parameters of a nano structured line grating, we fit a finite element numerical model to an experimental data set by using the Bayesian target vector optimization method. Gaussian process surrogate models are trained during the reconstruction. Afterwards, we employ a Markov chain Monte Carlo sampler on the surrogate models to determine the full model parameter distribution for the reconstructed model parameters. The choice of numerical discretization parameters, like the polynomial order of the finite element ansatz functions, impacts the numerical discretization error of the forward model. In this study we investigate the impact of numerical discretization parameters of the forward problem on the reconstructed parameters as well as on the model parameter distributions. We show that such a convergence study allows to determine numerical parameters which allow for efficient and accurate reconstruction results.

Keywords: Bayesian target vector optimization, Parameter reconstruction, Model accuracy, Least-squares, Bayesian optimization, Markov chain Monte Carlo.

1 Introduction

In the field of optical nano metrology dimensions of samples which are structured at the nanoscale are quantified by observing how the sample interacts with impinging light of precisely defined properties [1]. This is of particular interest in semiconductor manufacturing, where feature sizes need to be controlled on a level much smaller than the wavelength of light in the visible spectrum [2, 3, 4]. Various setups are used, where, e.g., the interaction of light with the sample at different wavelengths, angles of incidence, polarizations, etc., is measured and analyzed [5, 6, 7, 8]. As the measured spectra do not directly reveal the geometrical parameters, a common solution is to create a parameterized model of the measurement process. This model is also

referred to as a forward problem. Assuming that the model accurately represents the measurement process, it can then be fit to the experimental measurement. The parameters resulting from the fit can then be used to indirectly explain the, e.g., geometrical, parameters of the investigated structure [9]. Many different fitting methods have been shown to be capable of solving this inverse or parameter reconstruction problem. These include local methods such as the Gauss-Newton scheme or the Levenberg-Marquardt algorithm [10, 11], Nelder-Mead or L-BFGS-B [12], or heuristic global methods like particle swarm optimization [13, 14] or differential evolution [15, 16]. One can also maximize the appropriate likelihood function using Markov chain Monte Carlo (MCMC) sampling methods [17].

Due to the generally complex nature of the measurement process, the parameterized models are typically implemented using numerical methods. Such numerical models have two sets of parameters: a set of physical parameters which encode physical quantities (such as geometrical parameters), and a set of numerical parameters which control the numerical approximation accuracy. Selecting appropriate numerical parameters is an integral part of the creation of numerical models. They are usually determined by means of a convergence study. Here, the numerical parameters are systematically varied while the physical parameters are kept fixed. The model output is then compared to a reference solution which is assumed to be very accurate. The numerical parameters are chosen such that (i) a convergence trend of the output can be seen and (ii) a desired accuracy is reached. Appropriate numerical parameters can trade off numerical accuracy and computational costs, but more importantly assert that the results of the model are reliable.

In this article we extend this approach, and additionally (i) determine a least-square estimate by performing complete parameter reconstructions, using a set of different numerical parameters, and (ii) for a subset of the considered numerical parameters determine the full (potentially non-Gaussian) model parameter distribution by means of a MCMC sampling method. Naïvely this is prohibitively expensive for any model for

which the evaluation requires more than a few seconds of wall time. The task becomes feasible by using an approach centered around Gaussian processes (GPs) [18]. GPs are machine learning *surrogate* models that can be trained on observations of the actual model. After they are trained they can serve as a cheap-to-evaluate predictor for the actual model, and can therefore also be used instead of them. For parameter reconstructions, here we employ the Bayesian target vector optimization (BTVO) scheme [19], afterwards we apply a MCMC sampler to infer the full model parameter distribution from the GP surrogates trained during the parameter reconstruction. For an accurate determination of the full model parameter distribution, the surrogate model has to be a faithful representation of the actual model within a certain parameter space. Therefore, prior to the MCMC sampling, a surrogate refinement stage is entered in which the fidelity of the GP surrogates is increased by adding observations of the actual model in the region to be sampled by the MCMC sampler. The complete parameter reconstruction workflow including MCMC sampling is sketched in Figure 1.

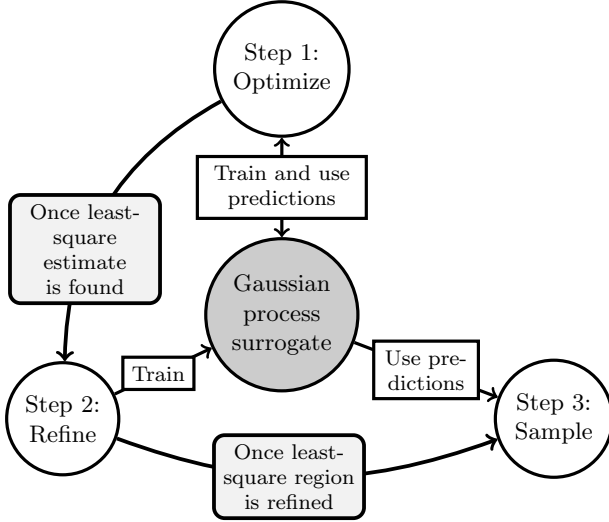


Figure 1: A schematic of the complete three-step reconstruction process. At each step a Gaussian process surrogate model is trained and/or its predictions are used. In the Step 1, the Bayesian target vector optimization scheme is applied and a least-square estimate of the forward problem is determined. In Step 2, the surrogate model trained during Step 1 is refined, and the fidelity in the region around the found least-square estimate is increased. Finally, in Step 3, the refined surrogate model is sampled using a Markov chain Monte Carlo method, to determine the full distribution of the model parameters.

This article is organized as follows. Section 2 contains the theoretical background. We discuss parameter reconstructions and finding a least-square estimate, which includes a simple estimate for model parameter uncertainties based on the Jacobian matrix. We then review the BTVO method and discuss how the GP surrogates trained during a BTVO run can be used for MCMC sampling. Finally, we briefly discuss ways of

controlling the accuracy of the numerical model. In Section 3 we investigate the impact of a proper or improper choice of numerical parameters. We revisit a parameter reconstruction problem, in which a line grating is investigated in a Grazing Incidence X-Ray Fluorescence (GIXRF) measurement [19, 20]. We first perform a conventional convergence analysis. For each of the numerical parameters considered in the convergence analysis we then determine a least-square estimate by performing a parameter reconstruction using the BTVO. Finally, for a subset of the numerical parameters considered we determine the full model parameter distribution using the surrogate aided MCMC approach.

2 Background

We briefly review the theoretical fundamentals for parameter reconstructions using the Bayesian target vector optimization method [19]. Moreover, we briefly discuss ways of controlling the level of accuracy in FEM simulations.

2.1 Parameter reconstructions and the least-square problem

Parameter reconstruction problems in optical metrology are often least-square type problems. The task here is to fit the K outputs of a parameterized forward model function $\mathbf{f}(\mathbf{p})$ to a set of experimental measurements $\mathbf{t} = (t_1, \dots, t_K)^T$, with $\mathbf{p} \in \mathcal{X} \subset \mathbb{R}^N$ and $\mathbf{f} : \mathcal{X} \rightarrow \mathbb{R}^K$. We assume that the forward model function is a good approximation of the measurement process, and that model errors can therefore be neglected. Furthermore the forward model function is treated as a black box that simply maps input parameters \mathbf{p} to output values $\mathbf{y} = \mathbf{f}(\mathbf{p})$. Here we assume that \mathbf{f} is once differentiable and that each of the K outputs can be modeled by GPs.

For a *true* parameter \mathbf{p}_t we assume that the output of the model $\mathbf{f}(\mathbf{p}_t)$ equals the experimental dataset plus a Gaussian noise contribution with zero-mean and variance η_k^2 , i.e.,

$$t_k = f_k(\mathbf{p}_t) + \varepsilon_k \quad \text{with} \quad \varepsilon_k \sim \mathcal{N}(0, \eta_k^2). \quad (1)$$

Finding a good least-square estimate (LSQE) for the unknown true parameter can be considered an optimization problem. This is often solved by minimizing the residual sum of squares

$$\chi^2(\mathbf{p}) = \sum_{k=1}^K \frac{(f_k(\mathbf{p}) - t_k)^2}{\eta_k^2}, \quad (2)$$

i.e., by finding

$$\mathbf{p}_{\text{LSQE}} = \arg \min_{\mathbf{p} \in \mathcal{X}} \chi^2(\mathbf{p}). \quad (3)$$

A solution for Equation (3) can be found, e.g., by using least-square methods such as Levenberg-Marquardt

(LM) [21,22,23] or the BTVO method presented in Section 2.2.

Further, also the uncertainties of the model parameters are of interest. For least-square methods such as LM one can use the Jacobian matrix at the least-square estimate to calculate the covariance matrix $\mathbf{Cov}(\mathbf{p}_{\text{LSQE}})$, which can then be used to determine Gaussian uncertainty bands ϵ_{LSQE} , i.e., uncertainties in terms of symmetric 1σ intervals around \mathbf{p}_{LSQE} [24, 25, 26].

2.2 A Bayesian optimization approach to parameter reconstructions

Bayesian optimization (BO) methods [27, 28] are sequential optimization methods that can be very efficient for globally optimizing expensive black box functions [12, 28, 29]. At each iteration during the optimization process a stochastic machine learning surrogate model – most often a GP [18, 30] – is trained using all previously observed values of the forward model. GPs are usually much cheaper to evaluate than the model function itself.

By considering all previous observations a global model of the expensive forward model function is created. This gives BO methods an advantage over conventional optimization methods, that often only create a local model of the forward model, e.g., in the form of a Hessian (e.g., for L-BFGS-B [31]) or Jacobian (e.g., Gauss-Newton type methods [32]) at the point of evaluation.

In BO the optimization typically happens in a cyclic fashion that repeats in each step of the optimization. First the GP surrogate is trained on the observations of the model function that have been seen in all previous iterations. Afterwards the length scales of the GP are optimized such that they best describe the training data. This *hyperparameter optimization* is usually computationally rather expensive and can also be done sparsely, e.g., every M_{Hyp} iterations. Now the GP surrogate can be used as a predictor or interpolator of the training data. Finally an acquisition (or utility) function is maximized that follows a specific strategy and uses the predictions made by the GP for finding a point in the parameter space that should be sampled next in order to achieve the goal of the optimization. This new sample and the associated black box function value are then added to the training data for the next iteration.

Each iteration in the optimization thus contains multiple smaller optimization steps. This is numerically expensive and the reason why BO methods are usually reserved for model functions for which the calculation of point values is at least as expensive as one of the nested optimization cycles.

This approach can be adopted to solve least-square parameter reconstruction problems. In the References [19, 33] K independent GPs are trained on the K outputs of the vector valued forward model function $\mathbf{f}(\mathbf{p})$. At each iteration in the optimization an appropriate utility function then generates new sample candidates that can lead to an improvement over

the currently best χ^2 value. The Bayesian target vector optimization (BTVO) scheme [19] implements several key performance improvements that make the method perform well even for a large number K of components in the forward model function $\mathbf{f}(\mathbf{p})$.

In the following we will first briefly review GPs as essential building blocks for the BTVO scheme, and then give an overview over the scheme itself and the improvements over the approach taken by Uhrenholt and Jensen [33].

2.2.1 Gaussian processes

A GP [18, 30] is a stochastic machine learning surrogate model that is defined on continuous domain \mathcal{X} . GPs can best be understood as an extension of finite dimensional multivariate normal distributions (MVNs) to an infinite dimensional case. A MVN is completely specified by a mean vector $\boldsymbol{\mu}$ and a covariance matrix $\boldsymbol{\Sigma}$. For a GP these are replaced by a continuous mean function $\mu : \mathcal{X} \rightarrow \mathbb{R}$ and a covariance kernel function $k : \mathcal{X} \times \mathcal{X} \rightarrow \mathbb{R}$. Frequent choices [12] which are also applied in this article are a constant mean function $\mu(\mathbf{p}) = \mu_0$ and a Matérn $5/2$ covariance kernel function [27], i.e.,

$$k(\mathbf{p}, \mathbf{p}') = \sigma_0 \left(1 + \sqrt{5}r + \frac{5}{3}r^2 \right) \times \exp \left(-\sqrt{5}r \right), \quad (4)$$

$$\text{where } r = \sqrt{\sum_{n=1}^N \left(\frac{p_n - p'_n}{l_n} \right)^2}. \quad (5)$$

GPs are parameterized by hyperparameters $\{\mu_0, \sigma_0, l_1, \dots, l_N\} \in \mathbb{R}$. These are chosen to maximize the likelihood of the observations. Once a GP has been trained on M observations of a function $f : \mathcal{X} \rightarrow \mathcal{Y} = \mathbb{R}$, i.e., on $\mathbf{Y} = [f(\mathbf{p}_1), \dots, f(\mathbf{p}_M)]^T$, it can be used to predict a normal distribution at each point \mathbf{p}_* in the parameter space,

$$\hat{f}(\mathbf{p}_*) \sim \mathcal{N}(\hat{y}(\mathbf{p}_*), \hat{\sigma}^2(\mathbf{p}_*)).$$

For the parameter dependent predicted mean $\hat{y}(\mathbf{p}_*)$ and variance $\hat{\sigma}^2(\mathbf{p}_*)$ of the GP we have

$$\begin{aligned} \hat{y}(\mathbf{p}_*) &= \mu_0 + \mathbf{k}^T(\mathbf{p}_*)\mathbf{K}^{-1}[\mathbf{Y} - \mu_0\mathbf{1}], \\ \hat{\sigma}^2(\mathbf{p}_*) &= \sigma_0^2 - \mathbf{k}^T(\mathbf{p}_*)\mathbf{K}^{-1}\mathbf{k}(\mathbf{p}_*), \end{aligned}$$

where the covariance kernel function $k(\mathbf{p}, \mathbf{p}')$ is used to compute $\mathbf{k}(\mathbf{p}_*) = [k(\mathbf{p}_*, \mathbf{p}_1), \dots, k(\mathbf{p}_*, \mathbf{p}_M)]^T$ and $(\mathbf{K})_{ij} = k(\mathbf{p}_i, \mathbf{p}_j)$.

2.2.2 Bayesian target vector optimization

In order to solve the problem of determining \mathbf{p}_{LSQE} the BTVO scheme trains K independent GP surrogates with the K discrete outputs of the parameterized forward model $\mathbf{f}(\mathbf{p})$. An alternative approach is to train a single multi-output GP [34, 35] that is capable of predicting all K outputs at the same time. Naïvely the size of the covariance matrix grows by a factor of K at each iteration. For models with a small

number of channels this can be a viable option. For forward models with $K \sim \mathcal{O}(100)$ this can however present an issue, as the covariance matrix has to be inverted at each iteration at a cost of approximately $\mathcal{O}(K^3)$ FLOPS [26]. This high complexity can be reduced drastically by e.g. choosing a separable covariance kernel [34]. It has successfully been applied in Ref. [36], where a separable kernel was employed to account for correlations between model output channels in a least-square regression problem.

Naïvely, the hyperparameters of each GP have to be optimized individually. In the BTVO this is avoided by sharing the covariance matrix between all K GPs. This approach can be motivated by the assumption that many problems considered one performs, e.g., an angular or wavelength/energy scan for the same model parameters. Here one can assume that the length scales of each of the scanned parameters are similar. Therefore, at each iteration, only one comparatively small covariance matrix has to be inverted instead of K . The predicted normal distributions of each GP are then combined in the calculation of a stochastic chi-square predictor variable $\hat{\chi}^2(\mathbf{p})$, i.e.,

$$\hat{\chi}^2(\mathbf{p}) = \sum_{k=1}^K \frac{(\hat{f}_k(\mathbf{p}) - t_k)^2}{\eta_k^2}. \quad (6)$$

Since this random variable is composed of a sum of non-central normal distributions with non-unit variance, it follows a *generalized* chi-square distribution. In principle it is possible to calculate values for this distribution, this can however be very costly [37, 38]. In order to efficiently incorporate this distribution into the optimization scheme it is therefore approximated twice, such that its values are ultimately given by a parameterized normal distribution. This allows for an efficient implementation of the lower confidence bound (LCB) acquisition function [33] employed in the BTVO method.

Unfortunately, these approximations introduce numerical issues within the acquisition function. For a large number of channels K in the forward model the probability of finding chi-square values smaller than the current optimum very rapidly tends toward zero as the iterations increase [19]. This reduces the exploratory nature of the scheme quite drastically, as the acquisition function will generally only generate sample candidates close to previously sampled positions. In order to restore the exploratory nature of the scheme the BTVO instead uses a modified parameterization of the approximated probability distribution [19].

The BTVO method has been shown to be capable of outperforming established parameter reconstruction methods, and that it can reach reconstructed parameters in fewer iterations than, e.g., LM [19]. The method has since been applied to other expensive parameter reconstruction problems [39].

Naturally, one could use the conventional BO method to solve the least-square problem directly [12]. The BTVO scheme has two major advantages over this

naïve approach. First, by training a stochastic model for each component of the model function a lot of information is retained about the interplay of the K channels of the model function. By determining the residual *sum of squares* (where both summing up and squaring erase information) invaluable information is lost that can provide one with an advantage during optimization. And second, the employed chi-square distribution used in the BTVO better matches the minimized chi-square value. During a parameter reconstruction with the conventional BO a single GP is trained on chi-square values (defined on \mathbb{R}^+ , including zero) that predicts a normal distribution (defined on \mathbb{R}). In regions where the training data approaches zero it can happen that the predictions of the GP will be wrong or at least inaccurate. Critically, this is precisely the case when the goal of the optimization of finding parameter values with small chi-square values is reached. Both of these issues lead to sub-optimal optimization performance.

2.3 Efficient determination of the model parameter distribution via Markov chain Monte Carlo

Since derivatives of the forward model w.r.t. all model parameters are easily calculated using GPs [40] it is possible to, similar to, e.g., LM, determine Gaussian uncertainty bands ϵ_{LSQE} by means of the covariance matrix $\mathbf{Cov}(\mathbf{p}_{\text{LSQE}})$. Linear correlations between the model parameters are also easily revealed [24, 25].

A much more informative quantity is the *full* model parameter distribution, from which one can extract the model parameter uncertainties in terms of 16 %, 50 % (i.e., the median), and 84 % percentiles, as well as potentially non-linear correlations between the various model parameters. The full model parameter distribution can generally not be established in an analytical fashion. Instead it is often determined by means of sampling methods, such as a Markov chain Monte Carlo (MCMC) [41, 42, 43] ansatz.

For parameter reconstruction problems, the MCMC sampler draws samples from the likelihood function for K independent normally distributed random variables [44]

$$\mathcal{L}(\mathbf{p}) = \prod_{k=1}^K \frac{1}{\sqrt{2\pi\eta_k^2}} \exp\left(-\frac{1}{2} \frac{(f_k(\mathbf{p}) - t_k)^2}{\eta_k^2}\right), \quad (7)$$

and uses them to construct one or more Markov chains, i.e., chains of samples from the domain of the forward model. The equilibrium distribution of the samples in these chains resemble the desired model parameter distribution. This distribution can, e.g., be visualized and analyzed by constructing histograms of the the samples in the chains.

MCMC allows to even extend the least-square ansatz of constant measurement errors [25], and instead fit a more complex error model to the measured data. It is therefore an invaluable method in many areas of science and engineering, not just for metrology applications.

In order to construct the equilibrium distribution the likelihood function is evaluated often several tens of thousand of times. This can make the method unattractive from a resource standpoint if the forward model $\mathbf{f}(\mathbf{p})$ in the likelihood is expensive to evaluate. Using a trained surrogate model instead of the actual forward model can lessen the resource impact drastically, since their evaluation is often orders of magnitude faster than the forward model. Ref. [19] propose to use the GP surrogates trained during an optimization run with the BTVO scheme.

An issue that arises when training these surrogate models is that one has to assert that the model possesses a sufficient degree of fidelity in the investigated region, i.e., around the least-square estimate \mathbf{p}_{LSQE} . For the surrogates trained during a BTVO run we can assume that they are trained in the region from which the least-square estimate was found. To ensure that the entire region is trained sufficiently well, a refinement stage is entered in which parameter samples are drawn from the normal distribution $\mathcal{N}(\mathbf{p}_{\text{LSQE}}, \mathbf{Cov}(\mathbf{p}_{\text{LSQE}}))$ and used to evaluate the forward model $\mathbf{f}(\mathbf{p})$. The results are used to train the surrogate further. This refinement process is stopped once the predicted variance of the GPs is below a certain threshold [19].

The actual MCMC sampling of the GP surrogate of the forward model is performed post-refinement using `emcee` [45]. The created chains are analyzed and visualized using `corner.py` [46], thereby revealing the individual marginal model parameter distributions, its 16 %, 50 % (i.e., the median), and 84 % percentiles, as well as potential non-linear correlations between the model parameters.

2.4 Numerical solution of the forward model

The parameterized forward model $\mathbf{f}(\mathbf{p})$ maps input points \mathbf{p} from the parameter space to output values \mathbf{y} . These are obtained by solving the linear, time-harmonic Maxwell’s equations for scattering problems. In general, solutions for this type of problem cannot be found analytically. Therefore a numerical solver based on the finite element method (FEM) [47] is employed for obtaining solutions. The solver used in this article is `JCMSuite` [48, 49].

The geometry of the investigated scattering problem is discretized in space and thus approximated by a mesh of non-overlapping discrete elements (e.g., triangles for a problem in two dimensions). On these discrete elements the fields of Maxwell’s equations are expanded into a set of polynomial ansatz functions. This allows to formulate the problem of finding a solution to the problem in terms of algebraic equations, which can be tackled efficiently using numerical methods.

Two ways of controlling the numerical accuracy of the solution of the problem are (i) controlling the size h of the discrete elements used in the mesh, and (ii) varying the number or degree p of the polynomial ansatz functions. Both, reducing the size of the elements h and increasing the polynomial degree p increases the

resolution of the field expansion, i.e., reduces the numerical discretization error. This naturally also increases the resource demand, since more quantities need to be calculated when finding a solution. It is therefore important to find a balance between the numerical parameters h and p , and the required accuracy of the solution.

3 Computer experiments

We have used the BTVO method and the associated surrogate aided MCMC sampling approach to investigate the influence of the accuracy of an underlying FEM model on a parameter reconstruction. Here, the accuracy of the FEM model was controlled by varying the polynomial degree p .

The parameter reconstruction is performed by fitting the FEM model to an experimental data set. This data set was recorded during a Grazing Incidence X-Ray Fluorescence (GIXRF) experiment, performed by the PTB at the BESSY II light source in Berlin [50]. The measurement process and the FEM model is briefly discussed in Section 3.1. We have previously reported on the technical details on the BTVO method and used the same data set and model to demonstrate the method [19].

In our computer experiments we conducted a convergence study of the FEM model, where we observed how the simulated output of the model changes for different polynomial degrees $p \in \{2, \dots, 7\}$. We compared each result to a reference solution obtained using $p_{\text{ref}} = 8$.

For each of the polynomial degrees p considered in the convergence study we then performed a parameter reconstruction benchmark. Here, six independent parameter reconstructions using the BTVO method were performed for each p . The results at each iteration were compared to a trusted reference solution.

Finally, we have refined a small subset of the surrogates for different p created during the optimization benchmarks. Using these refined surrogates we have then determined the full model parameter distribution using the surrogate aided MCMC sampling approach.

All experiments were performed on the High Throughput Computing cluster at the Zuse Institute Berlin, on a Dell PowerEdge C6520 rack server with two Intel Xeon Gold 6338 processors, yielding 64 cores or 128 threads. The nodes were equipped with 1024 GB of RAM. The simulations were set up to use all available threads. The `JCMSuite` version employed was 5.2.4. The optimizer used in the experiments was shipped with the solver.

3.1 The experimental dataset and the FEM model

Grazing Incidence X-Ray Fluorescence (GIXRF) [20] is a destruction free indirect optical measurement method that can be used to determine geometrical as well as material parameters of periodically nano-structured samples. The investigated grating is illuminated with

monochromatic light in the X-ray regime, which penetrates the sample material to some extent. The reflected light interferes with the incident light and forms an X-ray standing wave field, which can locally increase light-matter interaction within the sample material. A portion of the incident energy is absorbed by the sample, but most is ultimately given off again in the form of a fluorescence spectrum. This is integrated and recorded by a calibrated silicon drift detector. The recorded signal depends very strongly on the incident angle, the sample material, as well as the sample geometry.

Exploiting the strong angular dependence of the fluorescence signal, an angular scan is performed over 208 discrete incidence angles, using X-ray light with an energy of 520 eV.

To reconstruct the experimental conditions and geometrical parameters of the periodic sample, a parameterized FEM model of the measurement process is created using the Maxwell solver **JCMSuite**. In it the electromagnetic fields of the X-ray standing wave field are simulated on a periodic unit cell of the geometry, and the modified 2D Sherman equation is subsequently used to calculate the fluorescence signal. This is done for each of the angles used in the angular scan of the experiment. The model function contains ten free parameters. Of these, seven are geometrical (e.g., the critical dimension), two are there to account for uncertainties in the incidence angles, and one is used to scale the simulated intensities to the experimental intensities.

We have previously reported on the data set [19]. For more information about the numerical model, a plot of an exemplary unit cell geometry, the complete parameters and parameter ranges, and the measured GIXRF signal, we refer the reader to Ref. [19].

3.2 Model convergence

In the model convergence analysis we investigate the convergence of the simulated fluorescence intensities for difference polynomial degrees p , for each of the angles θ considered in the experiment. To do this, a random model parameter \mathbf{p} from the allowed parameter domain was generated and used to evaluate the different p discretizations of the FEM model with. We chose $p \in \{2, \dots, 7\}$, and compared the simulated fluorescence intensities to a reference solution generated with a FEM model with $p_{\text{ref}} = 8$. The largest allowed side length of an element in the geometry discretization was set to $h = 5$ nm.

The convergence is determined by calculating the absolute value of the relative difference to the reference solution, i.e., as

$$\Delta f_p(\mathbf{p}) = \frac{|f_p(\mathbf{p}) - f_{\text{ref}}(\mathbf{p})|}{f_{\text{ref}}(\mathbf{p})}. \quad (8)$$

This value is given for the different angles θ in Figure 2 (left), as well as a median for each p in Figure 2 (right). Additionally, Figure 2 (right) serves as a color guide for most of the plots presented in this article, as the colors

for each p are identical to the colors in the figures that use color to differentiate between datasets.

Looking at the median representation of the convergence analysis in Figure 2 (right) we see a clear convergence trend for $p \geq 4$, with decreasing errors as p increases. The discretizations $p = 2$ and $p = 3$ stand out, as the median values deviate from the trend line towards much larger errors. This can also be seen in Figure 2 (left).

We see that for $p = 2$ (the blue line) the angle resolved difference is much more irregular than, e.g., for $p = 3$ (the orange line). Especially for angles $\theta \rightarrow 90^\circ$ we observe many data points that approach very small values $\Delta f_{p=2}(\mathbf{p}) \rightarrow 0$. This suggests that the signed numerator in $\Delta f_{p=2}(\mathbf{p})$, i.e., $f_{p=2}(\mathbf{p}) - f_{\text{ref}}(\mathbf{p})$, undergoes a sign change for these angles. This does also occur for $p > 2$, however not as frequently. This, together with the deviation from the trend line indicates that results from a FEM model with $p = 2$ cannot be considered converged.

The angle resolved absolute relative difference for $p = 3$ (the orange line) is considerably smoother than for $p = 2$. However, similar to $p = 2$, the values for $\Delta f_{p=3}(\mathbf{p})$ are at least an order of magnitude larger than the values for $p \geq 4$. Moreover, the values $\Delta f_{p=3}(\mathbf{p})$ are almost always larger than $\Delta f_{p=2}(\mathbf{p})$, even though the accuracy is higher. For a converged model we would expect the opposite.

This behavior forces us to assume that the results obtained from a FEM model with $p = 2$ and $p = 3$ can not be considered converged. In contrast and restating what we said above, we consider results obtained with a FEM model using $p \geq 4$ as converged. Here, increasing the polynomial degree p results in smaller errors, which of course comes at the cost of more numerical complexity and CPU time spent on a solution.

When we compare the left and right plot of Figure 2, we see a discrepancy between the *apparent* median of the angle resolve difference figure and the actually calculated median on the right. This is due to the non-homogeneous density of the measured angles. The measurement *Grazing Incidence X-Ray Fluorescence* places a strong emphasis on small (or grazing) angles. Accordingly, the density of the measured angles is much greater for angles $\theta \rightarrow 90^\circ$. This yields a difference between a median that one would guess at visually, and a median that is actually calculated.

3.3 Benchmarks

For each of the polynomial degrees p considered in Section 3.2 we have performed an optimization benchmark, where we have run six independent optimizations starting from random starting points in the parameter space [19]. We have provided a budget of 250 iterations to each optimization for reaching the final reconstructed parameters. This budget was often not exhausted, as many trials found a good least-square candidate \mathbf{p}_{LSQE} in less than 150 iterations.

The metric used to measure convergence is the distance of the reconstructed parameter at each iteration

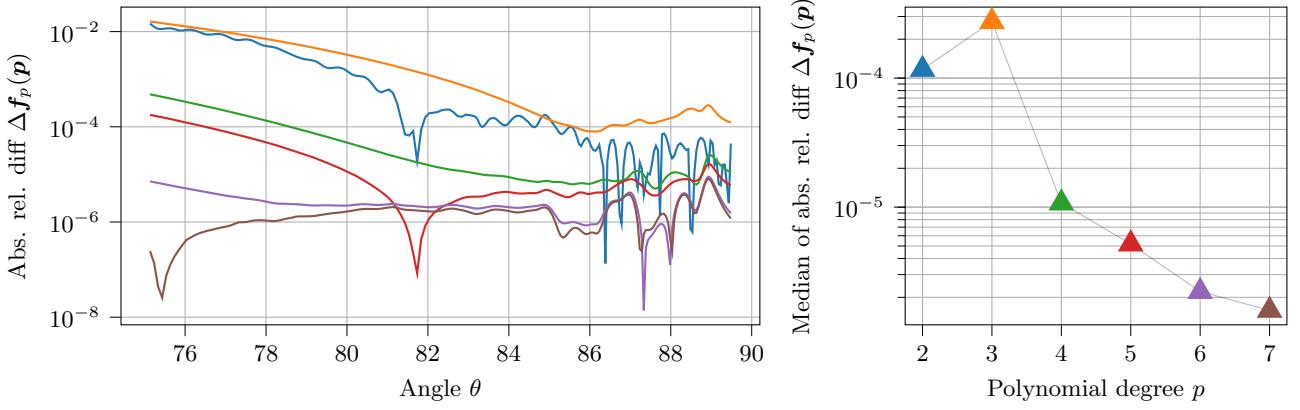


Figure 2: Convergence plot of the model for a random parameter \mathbf{p} in the parameter space. Shown is the absolute relative difference between the calculated model output for a polynomial degree $p \in \{2, \dots, 7\}$ and a reference model output with $p = 8$. The model outputs for $p = 2$ and $p = 3$ can not be considered converged. For $p = 2$ the model output fluctuates wildly w.r.t. the reference solution, and for $p = 3$ the difference from the reference solution is very large compared to the remainder of the considered polynomial orders. The absolute relative difference is defined as $\Delta \mathbf{f}_p(\mathbf{p}) = |\mathbf{f}_p(\mathbf{p}) - \mathbf{f}_{\text{ref}}(\mathbf{p})| / |\mathbf{f}_{\text{ref}}(\mathbf{p})|$, where division by the reference vector is meant component-wise. The right sub-figure serves as a color guide for the figures in this article.

m , \mathbf{p}_m , to a – at the time of the actual optimization unknown – reference parameter \mathbf{p}_{ref} , where each dimensional component of the compared parameters is weighted by the – at optimization time equally unknown – Gaussian uncertainties $\boldsymbol{\epsilon}_{\text{ref}}$. This distance is calculated as

$$d(\mathbf{p}_m) = \sqrt{\sum_{n=1}^N \left(\frac{\mathbf{p}_{m,n} - \mathbf{p}_{\text{ref},n}}{\boldsymbol{\epsilon}_{\text{ref},n}} \right)^2}. \quad (9)$$

These reference values are chosen to the best reconstructed parameter and the associated Gaussian uncertainty bands for the most accurate converged FEM model used in the optimization benchmarks, i.e., $\mathbf{p}_{\text{ref}} = \mathbf{p}_{\text{LSQE}}$ and $\boldsymbol{\epsilon}_{\text{ref}} = \boldsymbol{\epsilon}_{\text{LSQE}}$ obtained using $p = 7$. “Best” in this context means the parameter with the lowest χ^2 value for that particular p .

An obvious alternative metric that is often used when solving least-square problems is the $\chi^2(\mathbf{p}_m)$ value (or quantities proportional to it such as, e.g., the residual standard error (RSE)). This metric has the advantage that it is known immediately at time of optimization. We argue against using this metric. It can be misleading when performing parameter reconstructions since it relies on a fully converged model. We show in Figure 4 that the unconverged FEM models with $p = 2$ and $p = 3$ actually reach χ^2 values that are marginally smaller than the values that can be achieved with a fully converged FEM model with $p \geq 4$. Relying on the χ^2 metric can therefore lead to wrong conclusions and to falsely attributing importance to unconverged models. This is further visualized in Section 3.4.

From the six results for each p we have calculated the distance $d(\mathbf{p}_m)$. For each optimization we have then determined the cumulative minimum distance and finally calculated the median across each polynomial degree. These results are shown in Figure 3. The color

coding of the figure is identical to the one given in Figure 2 (right).

We observe that the converged models ($p \geq 4$) all reach a distance value $d \approx 0.1$ standard deviations to the trusted optimum \mathbf{p}_{LSQE} . This reproduces the results given in Ref. [19]. Here, the median results for $p = 6$ are clearly below this threshold, while the results for $p \in [4, 5, 7]$ remain slightly above it. The median distance results for $p = 2$ and $p = 3$ are only able to reach distance values of $d \gtrsim 1$. Here, the results for $p = 3$ are worse than the ones for $p = 2$.

As reference point for all optimizations performed in the benchmark we have chosen the parameter for $p = 7$ with the lowest χ^2 value. If instead we choose as reference point for each p the parameter with lowest χ^2 value for that p (e.g., for $p = 2$ we choose as reference point the best parameter obtained using $p = 2$), we see some improvements for the median results for $p = 2$ and $p = 3$. For $p = 3$ the median now also reaches a value of $d \approx 0.1$, and the median for $p = 2$ improves slightly to $d \approx 0.1$. In Section 2.3 we will see that for $p = 3$ this is due to a shift of the position of the parameter with lowest χ^2 value in the parameter space. The moderate improvement with $p = 2$ suggests a more complex function value landscape than for $p \geq 3$.

3.4 Evaluation of model parameter distributions

Finally, we inspect the function value landscape around the found least-square estimates for the FEM models with $p \in \{3, 4, 5\}$ more closely. For this, we use the surrogate aided MCMC approach detailed in Section 2.3 to sample the predicted likelihood function $\hat{\mathcal{L}}$.

Since the sampled likelihood function in Ref. [19] also included a simple error model, we take the same route to ensure comparable results. Therefore, we also

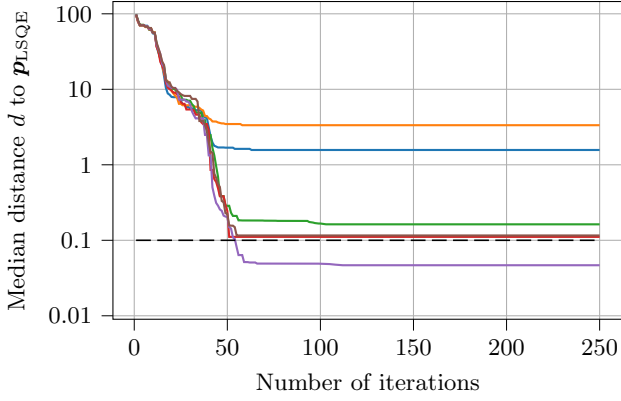


Figure 3: Progress of the parameter reconstruction for different polynomial degrees p . Shown is the median of six independent optimizations for each p . The used metric is the distance $d(\mathbf{p}_m)$ defined in Equation (9). The parameter reconstruction does not succeed when the employed model is not converged ($p = 2$ and $p = 3$), as the reconstructed parameters do not reach distances of less than one standard deviation from the trusted reference value. The parameter reconstruction succeeds when using a converged model (here, $p \geq 4$), where generally distances of approximately 0.1 standard deviations from the trusted optimum can be reached. For a color reference we refer the reader to Figure 2.

determined the distribution of the parameter η_c in the error model

$$\tilde{\eta}_k(\eta_c) = 2^{\eta_c} \cdot \eta_k \quad (10)$$

during the sampling process. This error model allows to scale the measurement errors of the experiment up or down. Accordingly, we draw samples from the predicted likelihood function

$$\hat{\mathcal{L}}(\mathbf{p}, \eta_c) = \prod_{k=1}^K \frac{1}{\sqrt{2\pi\tilde{\eta}_k^2(\eta_c)}} \exp\left(-\frac{1}{2} \frac{(\hat{f}_k(\mathbf{p}) - t_k)^2}{\tilde{\eta}_k^2(\eta_c)}\right). \quad (11)$$

We omit $p = 2$ from this analysis because we show that already the model for $p = 3$ is not converged, as well as $p \geq 6$, because we will already see very little difference between the model values for $p = 4$ and $p = 5$.

After the optimization benchmark using the BTVO we have six pre-trained surrogate models for each of the polynomial orders p considered. These surrogate models were trained on data originating from simulations of the respective FEM model; for a detailed discussion on the model and the parameters used we refer the reader to Ref. [19]. The surrogates can be used as cheap-to-evaluate accurate approximations of the expensive FEM model. Due to the random optimization starting points each of the surrogates contains different samples from the parameter space, that were investigated during the optimizations. For each $p \in \{3, 4, 5\}$ we select the surrogate model that has led to the smallest χ^2 value, and use this surrogate model as a starting

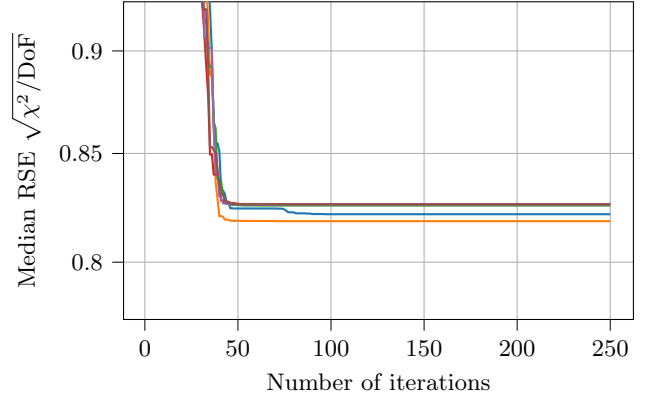


Figure 4: Illustrating example that the regression standard error (RSE) is not suited as a metric for comparing parameter reconstructions. The RSE can lead to wrong conclusions, as it implicitly assumes that the employed models are converged. Conversely, unconverged forward models can show behavior that is difficult to predict. Here we see that the model is able to reach a smaller RSE with (unconverged) $p = 2$ and $p = 3$. The RSE that can be reached using a converged model (i.e., for $p \geq 4$) is slightly larger. For a color reference we refer the reader to Figure 2.

point for the refinement process. For this pre-sampling refinement stage we provided a refinement budget of 250 additional samples that were used to increase the fidelity of the surrogate models in the proximity of the different \mathbf{p}_{LSQE} . After refinement, we then employed `emcee` [45] to construct 32 Markov chains containing 50 000 samples each, for the three p investigated.

The MCMC sampling region was restricted to a boxed region of three standard deviations ϵ_{LSQE} around the least-square estimate \mathbf{p}_{LSQE} . This was done because even after the refinement stage we can only assume that the surrogate model is sufficiently refined in a region close to the least-square estimate. In regions far away from training data the surrogate predictions revert back to the priors used in the construction of the GPs. This leads to difficult-to-predict behavior of the sampled predicted likelihood function, such that the MCMC sampler may falsely attribute importance to undersampled regions and therefore giving misleading results.

The results for a small subset of the marginal distributions of the reconstructed parameter are given in Figure 5. Therein we also give tabulated the median, as well as lower and upper standard deviation of the marginal model parameter distribution for the shown parameters and polynomial degrees p . The *complete* list of medians and lower/upper standard deviations, as well as the results for the fit error model, is given in Table 1. Note that for most of the additional parameters given in Table 1 we report similar results (within the reconstructed uncertainties) for all p considered.

For the displayed parameters we see that the model parameter distributions for the converged models ($p = 4$, and $p = 5$) are identical within the reconstructed

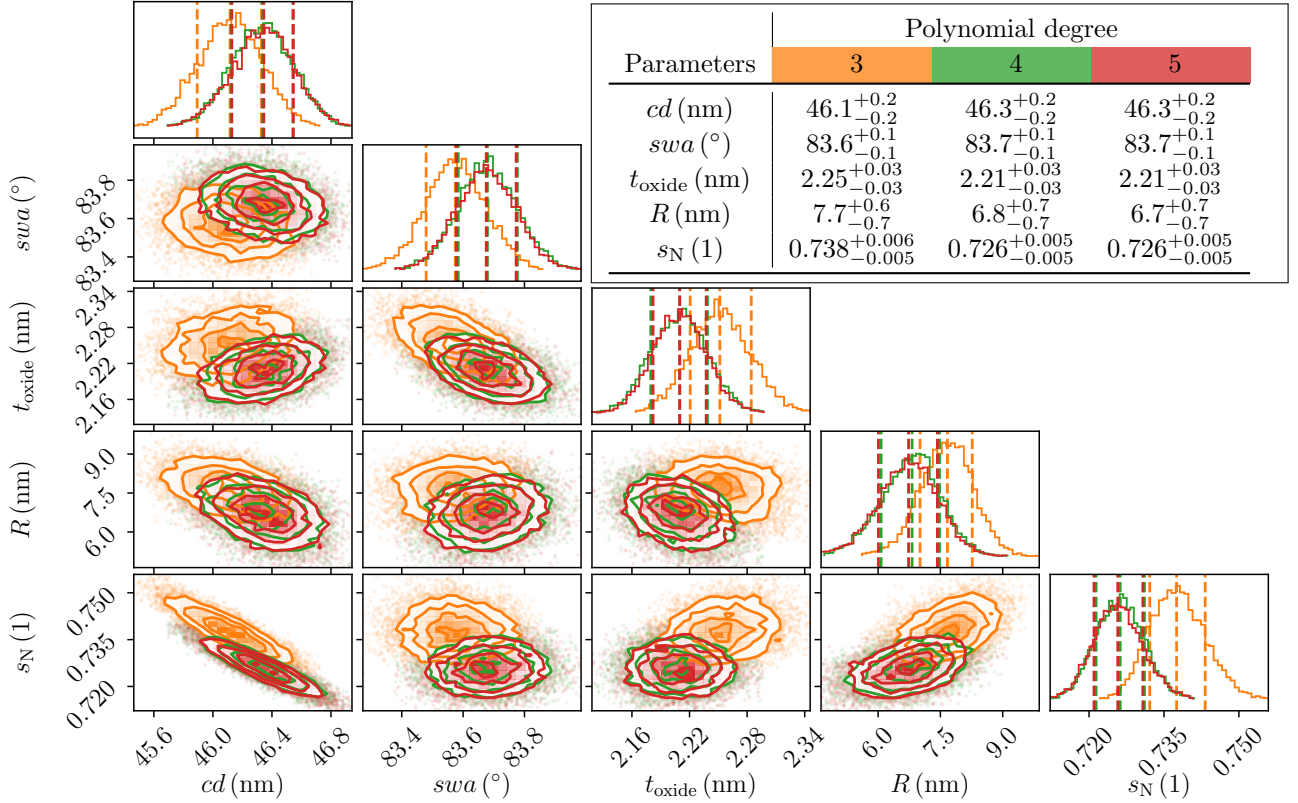


Figure 5: An excerpt of the reconstructed parameters and marginal probability distributions for the optimized model function for polynomial degrees $p \in \{3, 4, 5\}$. For $p = 3$ the model results have not converged yet, this leads to a different reconstructed optimum than for a converged model with $p \geq 4$. The inset table shows the numerical values for the reconstructed parameters and respective marginal distributions. The large numbers are the medians of the marginal distributions, while the values in the sub- and superscript are the values for the 16'th and 84'th percentile respectively.

model parameter uncertainties. In contrast to that, using an unconverged FEM model with $p = 3$ leads to a shift of more than one standard deviation of the median of the model parameter distribution for several components of the model parameter \mathbf{p} . The maximum likelihood estimate obtained by MCMC sampling for the parameter cd and swa with $p = 3$ are approximately one standard deviation smaller than the ones obtained with $p \geq 4$. Conversely, the model parameters t_{oxide} , R , and s_N are approximately one standard deviation larger. This explains why the median distance of the results for $p = 3$ in Figure 3 remain a distance of more than one standard deviation away from the $d \approx 0.1$ threshold. Similarly, it also explains why the use of an alternative reference value leads to $d \approx 0.1$ for $p = 3$, since only the position of the best reconstruction value appears to have shifted, while the general shape of the model parameter distribution is unaltered. The reconstructed uncertainties of the model parameters appear mostly unaffected by the use of an unconverged FEM model. Here, only the parameters R and t_{Sub} appear to have gained a small skewedness when using $p = 3$.

When using a converged FEM model we report the same model parameter distribution as Ref. [19] for the small subset given therein.

Finally, w.r.t. the fit parameter η_c of the simple error model Equation (10), we did not observe an impact of the proper or improper choice of the polynomial degree p on an over- or underestimation of the measurement errors.

3.5 Discussion

For the problem considered in this article the modeling differences between the polynomial degrees $p = 3$ and $p \geq 4$, described in Sections 3.2 to 3.4, are mostly seen as a shift in the distribution. Here, the median is shifted to a different position and a small skewedness is introduced to some of the model parameter marginal distributions.

We hypothesize that the shift in the median value for the different model accuracies is due to a very coarse sampling of the fields of Maxwells equations in the oxide layer of the mesh at the reconstructed model parameters. In simulations with a minimum mesh element size of $h = 5$ nm and an oxide layer thickness of $t_{\text{oxide}} \approx 2.2$ nm, this oxide layer will only be one element thick. Therefore, an already very small number of unknowns are reserved for calculating the effect of it on the simulated fluorescence signal. At the same time

this oxide layer is arguably among the most important components of the model, since it is the first part of the structure that the electromagnetic fields interact with.

This is exacerbated by the fact that any (even just minute) rotation of the sample during the measurement process will result in it being illuminated only from the top and the side. Additionally, for small (*grazing*) incidence angles one can assume that only the upper side of the structure is illuminated, since much of the incidence radiation is captured by other parts of the grating. In general, the bottom of the grating will not be illuminated strongly.

All of this is not captured in the model, but is contained in the experimental measurement. As such, the model parameters that control the top and top side of the structure will have a great importance on the reconstruction process. This is further exacerbated by the strong emphasis on grazing incidence angles $\theta \rightarrow 90^\circ$ during the experiment itself (by performing more experimental measurements there), and therefore for the least-square estimate.

The parameters that control the top and top side portion of the gratings unit cell structure are therefore very influential for the parameter reconstruction process. Here we have seen the largest difference in the reconstructed parameters. The two different parameterizations seen in Figure 5 and Table 1, i.e., (when going from $p = 3$ to $p = 4$) reducing the critical dimension cd and side wall angle swa while increasing the radius R and the thickness of the oxide layer t_{oxide} , approximately keep the amount of material in the oxide layer constant. In their respective accuracy setting of $p = 3$ and $p \geq 4$ they both apparently yield similar physical behavior, despite being several standard deviations (in reconstructed uncertainties) apart from each other.

4 Conclusion

We have presented an analysis of the impact of a properly or improperly chosen polynomial degrees p in a FEM model during a parameter reconstruction. This polynomial degree determines the accuracy, and as such the convergence, of the FEM model.

We have investigated the p convergence of the FEM model and identified different p for which the model results can be assumed to be converged, but also p for which we can expect model behavior that is difficult to predict.

This difficult to predict behavior had manifested itself in apparently better reconstruction results, especially when using inappropriate parameter reconstruction metrics such as the RSE.

Finally, we were able to make use of a surrogate aided MCMC approach to show that in this particular FEM model the improperly chosen polynomial degree $p = 3$ resulted in a shift of the parameter reconstruction result from the converged parameter reconstruction result for $p \geq 4$.

This article highlights the importance of using prop-

erly converged models in parameter reconstructions. It also stresses that ignorance about the state of model convergence can result in falsely attributing importance to unconverged results.

5 Conflicts of Interest

The authors declare no conflict of interest.

6 Acknowledgements

This project has received funding from the German Federal Ministry of Education and Research (BMBF, project number 05M20ZAA, siMLopt; project number 01IS20080A, SiM4diM; Forschungscampus MODAL, project number 05M20ZBM). This project has received funding from the EMPIR programme co-financed by the Participating States and by the European Union's Horizon 2020 research and innovation programme (project 20IND04 "ATMOC"; project 20FUN02 "POLIGHT"). The authors gratefully acknowledge the scientific support and HPC resources provided by the NHR center at ZIB. NHR funding is provided by federal and Berlin state authorities.

A Table with complete reconstructed distribution

Table 1 shows a listing of the percentiles of the full model parameter distribution for the polynomial degrees $p \in \{3, 4, 5\}$.

References

- [1] A. C. Diebold, "Nanoscale characterization and metrology," *J. Vac. Sci. Technol. A*, vol. 31, p. 050804, 2013.
- [2] N. G. Orji, M. Badaroglu, B. M. Barnes, C. Beitia, B. D. Bunday, U. Celano, R. J. Kline, M. Neisser, Y. Obeng, and A. Vladar, "Metrology for the next generation of semiconductor devices," *Nat. Electron.*, vol. 1, pp. 532–547, 2018.
- [3] A. J. den Boef, "Optical wafer metrology sensors for process-robust CD and overlay control in semiconductor device manufacturing," *Surf. Topogr.*, vol. 4, p. 023001, 2016.
- [4] J. Endres, A. Diener, M. Wurm, and B. Bodermann, "Investigations of the influence of common approximations in scatterometry for dimensional nanometrology," *Meas. Sci. Technol.*, vol. 25, p. 044004, 2014.
- [5] R. L. Jones, T. Hu, E. K. Lin, W.-L. Wu, R. Kolb, D. M. Casa, P. J. Bolton, and G. G. Barclay, "Small angle X-ray scattering for sub-100 nm pattern characterization," *Appl. Phys. Lett.*, vol. 83, p. 4059, 2003.

Parameters	Polynomial degree		
	3	4	5
h (nm)	$89.6^{+0.4}_{-0.4}$	$89.5^{+0.4}_{-0.4}$	$89.5^{+0.4}_{-0.4}$
cd (nm)	$46.1^{+0.2}_{-0.2}$	$46.3^{+0.2}_{-0.2}$	$46.3^{+0.2}_{-0.2}$
swa ($^\circ$)	$83.6^{+0.1}_{-0.1}$	$83.7^{+0.1}_{-0.1}$	$83.7^{+0.1}_{-0.1}$
t_{oxide} (nm)	$2.25^{+0.03}_{-0.03}$	$2.21^{+0.03}_{-0.03}$	$2.21^{+0.03}_{-0.03}$
t_{groove} (nm)	$1.1^{+0.3}_{-0.3}$	$1.1^{+0.3}_{-0.3}$	$1.0^{+0.3}_{-0.3}$
R (nm)	$7.7^{+0.6}_{-0.7}$	$6.8^{+0.7}_{-0.7}$	$6.7^{+0.7}_{-0.7}$
t_{Sub} (nm)	$6.8^{+0.8}_{-0.9}$	$7.0^{+0.8}_{-0.9}$	$7.0^{+0.8}_{-0.9}$
s_N (1)	$0.738^{+0.006}_{-0.005}$	$0.726^{+0.005}_{-0.005}$	$0.726^{+0.005}_{-0.005}$
Δ_θ ($^\circ$)	$-0.099^{+0.003}_{-0.003}$	$-0.102^{+0.003}_{-0.003}$	$-0.102^{+0.003}_{-0.003}$
Δ_ϕ ($^\circ$)	$0.003^{+0.01}_{-0.009}$	$0.007^{+0.011}_{-0.009}$	$0.007^{+0.011}_{-0.01}$
η_c (1)	$0.002^{+0.074}_{-0.07}$	$0.002^{+0.073}_{-0.07}$	$0.002^{+0.073}_{-0.072}$

Table 1: A complete listing of the reconstructed model parameters and their distribution percentiles as determined by MCMC sampling of the refined surrogate model of the expensive model function shown in Figure 5. The color coding of the polynomial degree title cells matches the colors of the figures in the main article.

- [6] S. O’Mullane, N. Keller, and A. C. Diebold, “Modeling ellipsometric measurement of three-dimensional structures with rigorous coupled wave analysis and finite element method simulations,” *J. Micro. Nanolithogr. MEMS MOEMS*, vol. 15, p. 044003, 2016.
- [7] R. K. Attota, P. Weck, J. A. Kramar, B. Bunday, and V. Vartanian, “Feasibility study on 3-D shape analysis of high-aspect-ratio features using through-focus scanning optical microscopy,” *Opt. Express*, vol. 24, p. 16574, 2016.
- [8] V. Soltwisch, A. Haase, J. Wernecke, J. Probst, M. Schoengen, S. Burger, M. Krumrey, and F. Scholze, “Correlated diffuse x-ray scattering from periodically nanostructured surfaces,” *Phys. Rev. B*, vol. 94, p. 035419, 2016.
- [9] R. C. Aster, B. Borchers, and C. H. Thurber, *Parameter estimation and inverse problems*. Elsevier, 2018.
- [10] M. Hammerschmidt, M. Weiser, X. G. Santiago, L. Zschiedrich, B. Bodermann, and S. Burger, “Quantifying parameter uncertainties in optical scatterometry using Bayesian inversion,” *Proc. SPIE*, vol. 10330, p. 1033004, 2017.
- [11] R. B. Storch, L. C. Pimentel, and H. R. Orlando, “Identification of atmospheric boundary layer parameters by inverse problem,” *Atmospheric Environment*, vol. 41, no. 7, pp. 1417–1425, 2007.
- [12] P.-I. Schneider, X. Garcia Santiago, V. Soltwisch, M. Hammerschmidt, S. Burger, and C. Rockstuhl, “Benchmarking five global optimization approaches for nano-optical shape optimization and parameter reconstruction,” *ACS Photonics*, vol. 6, no. 11, pp. 2726–2733, 2019.
- [13] F. Pace, A. Santilano, and A. Godio, “Particle swarm optimization of 2D magnetotelluric data,” *Geophysics*, vol. 84, no. 3, pp. E125–E141, 03 2019.
- [14] M. Schwaab, E. C. Biscaia Jr, J. L. Monteiro, and J. C. Pinto, “Nonlinear parameter estimation through particle swarm optimization,” *Chemical Engineering Science*, vol. 63, no. 6, pp. 1542–1552, 2008.
- [15] F. Lobato, V. Steffen Jr, and A. S. Neto, “Estimation of space-dependent single scattering albedo in a radiative transfer problem using differential evolution,” *Inverse Problems in Science and Engineering*, vol. 20, no. 7, pp. 1043–1055, 2012.
- [16] A. A. Cavalini Jr, F. S. Lobato, E. H. Koroishi, and V. Steffen Jr, “Model updating of a rotating machine using the self-adaptive differential evolution algorithm,” *Inverse Problems in Science and Engineering*, vol. 24, no. 3, pp. 504–523, 2016.
- [17] A. F. Herrero, M. Pflüger, J. Puls, F. Scholze, and V. Soltwisch, “Uncertainties in the reconstruction of nanostructures in EUV scatterometry and grazing incidence small-angle X-ray scattering,” *Opt. Express*, vol. 29, pp. 35 580–35 591, 2021.
- [18] C. K. Williams and C. E. Rasmussen, *Gaussian processes for machine learning*. MIT Press, 2006.
- [19] M. Plock, K. Andriele, S. Burger, and P.-I. Schneider, “Bayesian target-vector optimization for efficient parameter reconstruction,” *Adv. Theory Simul.*, vol. 5, no. 10, p. 2200112, 2022.
- [20] A. Andriele, P. Hönicke, G. Gwalt, P.-I. Schneider, Y. Kayser, F. Siewert, and V. Soltwisch, “Shape- and Element-Sensitive Reconstruction of Periodic Nanostructures with Grazing Incidence X-ray Fluorescence Analysis and Machine Learning,” *Nanomaterials*, vol. 11, p. 1647, 2021.

- [21] K. Levenberg, “A method for the solution of certain non-linear problems in least squares,” *Q. Appl. Math.*, vol. 2, no. 2, pp. 164–168, 1944.
- [22] D. W. Marquardt, “An algorithm for least-squares estimation of nonlinear parameters,” *J. Soc. Indust. Appl. Math.*, vol. 11, no. 2, pp. 431–441, 1963.
- [23] R. Fletcher, “A modified Marquardt subroutine for non-linear least squares,” Atomic Energy Research Establishment, Harwell (England), Tech. Rep. AERE-R-6799, 1971.
- [24] M. H. Kutner, C. J. Nachtsheim, J. Neter, and W. Li, *Applied Linear Statistical Models*, 5th ed. McGraw-Hill Irwin, 2005.
- [25] T. Strutz, *Data Fitting and Uncertainty: A Practical Introduction to Weighted Least Squares and Beyond*. Vieweg and Teubner, 2011.
- [26] W. H. Press, S. A. Teukolsky, W. T. Vetterling, and B. P. Flannery, *Numerical Recipes: The Art of Scientific Computing*, 3rd ed. Cambridge University Press, 2007.
- [27] E. Brochu, V. M. Cora, and N. de Freitas, “A tutorial on Bayesian optimization of expensive cost functions, with application to active user modeling and hierarchical reinforcement learning,” *arXiv preprint, arXiv:1012.2599*, 2010.
- [28] D. R. Jones, M. Schonlau, and W. J. Welch, “Efficient global optimization of expensive black-box functions,” *J. Global Optim.*, vol. 13, pp. 455–492, 1998.
- [29] P.-I. Schneider, M. Hammerschmidt, L. Zschiedrich, and S. Burger, “Using Gaussian process regression for efficient parameter reconstruction,” *Proc. SPIE*, vol. 10959, p. 1095911, 2019.
- [30] R. Garnett, *Bayesian Optimization*. Cambridge University Press, 2023.
- [31] R. H. Byrd, P. Lu, J. Nocedal, and C. Zhu, “A limited memory algorithm for bound constrained optimization,” *SIAM J. Sci. Comp.*, vol. 16, no. 5, pp. 1190–1208, 1995.
- [32] P. Deuffhard, *Newton methods for nonlinear problems: affine invariance and adaptive algorithms*. Springer Science & Business Media, 2005, vol. 35.
- [33] A. K. Uhrenholt and B. S. Jensen, “Efficient Bayesian optimization for target vector estimation,” in *The 22nd International Conference on Artificial Intelligence and Statistics*. PMLR, 2019, pp. 2661–2670.
- [34] M. A. Alvarez, L. Rosasco, and N. D. Lawrence, “Kernels for vector-valued functions: A review,” *arXiv preprint arXiv:1106.6251*, 2011.
- [35] H. Liu, J. Cai, and Y.-S. Ong, “Remarks on multi-output Gaussian process regression,” *Knowl.-Based Syst.*, vol. 144, pp. 102–121, 2018.
- [36] K. Matsui, S. Kusakawa, K. Ando, K. Kutsukake, T. Ujihara, and I. Takeuchi, “Bayesian active learning for structured output design,” *arXiv preprint, arXiv:1911.03671*, 2019.
- [37] A. M. Mathai and S. B. Provost, *Quadratic forms in random variables: theory and applications*. Dekker, 1992.
- [38] A. A. Mohsenipour, “On the distribution of quadratic expressions in various types of random vectors,” Ph.D. dissertation, University of Western Ontario, 2012.
- [39] P.-I. Schneider, P. Manley, J. Krüger, L. Zschiedrich, R. Köning, B. Bodermann, and S. Burger, “Reconstructing phase aberrations for high-precision dimensional microscopy,” *Proc. SPIE*, vol. 12137, p. 121370I, 2022.
- [40] X. Garcia-Santiago, P.-I. Schneider, C. Rockstuhl, and S. Burger, “Shape design of a reflecting surface using bayesian optimization,” *J. Phys. Conf. Ser.*, vol. 963, p. 012003, 2018.
- [41] C. Andrieu, N. De Freitas, A. Doucet, and M. I. Jordan, “An introduction to MCMC for machine learning,” *Mach. Learn.*, vol. 50, no. 1, pp. 5–43, 2003.
- [42] C. Sammut and G. I. Webb, *Encyclopedia of machine learning*. Springer Science & Business Media, 2011.
- [43] J. Friedman, T. Hastie, R. Tibshirani *et al.*, *The elements of statistical learning*. Springer series in statistics New York, 2001, vol. 1, no. 10.
- [44] M. H. DeGroot and M. J. Schervish, *Probability and statistics*, 4th ed. Pearson, 2012.
- [45] D. Foreman-Mackey, D. W. Hogg, D. Lang, and J. Goodman, “emcee: The MCMC Hammer,” *Publ. Astron. Soc. Pac.*, vol. 125, no. 925, p. 306, 2013.
- [46] D. Foreman-Mackey, “corner.py: Scatterplot matrices in python,” *The Journal of Open Source Software*, vol. 1, no. 2, p. 24, 2016.
- [47] P. Monk, *Finite Element Methods for Maxwell’s Equations*. Oxford: Clarendon Press, 2003.
- [48] J. Pomplun, S. Burger, L. Zschiedrich, and F. Schmidt, “Adaptive finite element method for simulation of optical nano structures,” *Phys. Status Solidi B*, vol. 244, no. 10, p. 3419, 2007.
- [49] S. Burger, L. Zschiedrich, J. Pomplun, and F. Schmidt, “JCMsuite: An adaptive FEM solver for precise simulations in nano-optics,” in *Integrated Photonics and Nanophotonics Research and*

Applications. Optical Society of America, 2008, p. ITuE4.

- [50] V. Soltwisch, P. Hönicke, Y. Kayser, J. Eilbracht, J. Probst, F. Scholze, and B. Beckhoff, “Element sensitive reconstruction of nanostructured surfaces with finite elements and grazing incidence soft X-ray fluorescence,” *Nanoscale*, vol. 10, pp. 6177–6185, 2018.